ADVANCING EARTH AND SPACE SCIENCES

JGR Atmospheres

RESEARCH ARTICLE
10.1029/2026JD046315

Key Points:

- The weather research and forecast output-driven Makkonen model provides an effective method to monitor regional power line icing over the mountainous regions
- Adopting higher model horizontal resolution improves the simulation of near-surface air temperature, moisture, and icing thickness
- Simulations with the Morrison scheme perform better than using the Thompson scheme in simulating near-surface meteorology, and icing thickness

Correspondence to:
A. Huang and G. Wang,
anhuang@nju.edu.cn;
wanggy@swepdi.com

Citation:
Luo, J., Wang, G., Huang, A., Guo, X., Gu, C., Huang, S., & Ran, H. (2026). Performance evaluation of the Makkonen model driven by the output of the WRF model in simulating power line icing thickness in the mountainous regions of southwest Sichuan, China. *Journal of Geophysical Research: Atmospheres*, *131*, e2026JD046315. https://doi.org/10.1029/2026JD046315

Received 4 JAN 2026
Accepted 15 JUN 2026

Author Contributions:
Conceptualization: Anning Huang
Data curation: Jiangxin Luo, Xinchun Guo
Formal analysis: Jiangxin Luo, Anning Huang, Xinchun Guo, Chunlei Gu, Shuai Huang, Haitao Ran
Investigation: Jiangxin Luo, Guoyu Wang, Anning Huang
Methodology: Jiangxin Luo
Resources: Jiangxin Luo
Software: Jiangxin Luo
Supervision: Guoyu Wang, Anning Huang
Validation: Jiangxin Luo
Visualization: Jiangxin Luo
Writing – original draft: Jiangxin Luo, Guoyu Wang, Anning Huang, Xinchun Guo, Chunlei Gu, Shuai Huang, Haitao Ran

Performance Evaluation of the Makkonen Model Driven by the Output of the WRF Model in Simulating Power Line Icing Thickness in the Mountainous Regions of Southwest Sichuan, China

Jiangxin Luo[1,2], Guoyu Wang[2], Anning Huang[1,3], Xinchun Guo[2], Chunlei Gu[1], Shuai Huang[2], and Haitao Ran[2]

[1]School of Atmospheric Sciences, Nanjing University, Nanjing, China, [2]China Power Engineering Consulting Group, Southwest Electric Power Design Institute Co., Ltd., Chengdu, China, [3]Chinese Academy of Sciences, Qinghai Lake Comprehensive Observation Research Station, Gangcha, China

Abstract Power line icing frequently occurs in the mountainous regions of southwestern Sichuan, China, posing significant risks to power system operations. Numerical simulation offers an effective tool for predicting icing processes; however, the applicability of the Makkonen model driven by the output of the weather research and forecast (WRF) model in this region remains uncertain. In this study, a series of simulations were conducted using the WRF and Makkonen models with four nested domains (9, 3, 1, and 0.33 km) and two cloud microphysical schemes (Thompson and Morrison), based on eight observed icing events at Erlangshan station. Results show that the WRF output-driven Makkonen model can reasonably reproduce the icing process although the icing thickness is generally underestimated. Increasing the horizontal resolution can improve the simulations of near-surface air temperature and moisture, leading to more accurate icing estimates. This improvement is primarily attributed to a better representation of terrain effects, including enhanced ridge-induced cooling, wind acceleration, and orographic lifting, which promote the formation of super-cooled liquid water and increase collision and freezing efficiencies. Moreover, adopting the Morrison scheme produces larger icing thickness and shows better agreement with observations than using the Thompson scheme. This difference is mainly due to microphysical processes. Adopting the Morrison scheme increases rain number concentration and shifts the particle size distribution toward smaller droplets, thereby reducing the conversion efficiency of cloud water to precipitation and ice. As a result, more super-cooled liquid water is retained, enhancing icing growth and reducing model bias.

Plain Language Summary Power line icing is a common hazard in the mountainous regions of southwestern Sichuan, China, and can threaten the safe operation of power systems. This study evaluates how well numerical models can simulate icing and what factors control the prediction accuracy. We use the weather research and forecast model to provide meteorological data for an icing model and test two different cloud microphysical schemes using eight observed icing events. The results show that the model can capture the general icing process but tends to underestimate the icing thickness. Increasing the model resolution can improve the representation of complex terrain, which leads to more realistic simulations of air temperature, moisture, and airflow near mountain ridges. These improvements help produce more super-cooled liquid water and increase the efficiency of droplet collision and freezing, resulting in more accurate icing estimates. Meanwhile, the choice of cloud microphysical scheme is important. The Morrison scheme performs better than the Thompson scheme because it produces smaller cloud droplets and retains more liquid water in the atmosphere. This provides more material for icing formation on power lines. Overall, improving both model resolution and cloud physics representation can significantly enhance icing simulations in mountainous regions.

1. Introduction

Power line icing is a meteorological phenomenon in which supercooled liquid water or solid precipitation collides with and freezes upon the power line surface (Chang et al., 2007; Drage & Hauge, 2008; Poots, 2000). This process constitutes a major weather-related hazard, as the accumulated icing can cause power lines to sway, deform, or even fail, leading to operational disruptions and significant economic losses (Jiang et al., 2014; Niu et al., 2011).

Writing – review & editing: Jiangxin Luo, Guoyu Wang, Anning Huang, Xinchun Guo, Chunlei Gu, Shuai Huang, Haitao Ran

China is among the countries most severely affected by power line icing, with one of the highest occurrence rates worldwide (Sokolov et al., 2025; Watanabe, 1978). Studies indicate that between 1954 and 2006, more than 1,000 icing-related disasters were recorded across the country (Hu et al., 2006; Huang et al., 2005). The frequency of such events has shown a rapid increase following the expansion of high-voltage transmission networks (Guo et al., 2019; Li et al., 2008; Long et al., 2006; Wang, H. et al., 2023). A particularly severe series of icing disasters occurred successively in southern, southwestern, central, and eastern China from 10 January to 2 February 2008, causing extensive damage to transmission lines and towers and posing a serious threat to the safety and stability of the power system (Hou et al., 2009; Niu et al., 2011; Yang et al., 2008). In addition to this extreme event, frequent icing disasters have continued to occur in recent years, further highlighting their widespread and persistent impacts. For example, in 2011, a freezing rain and snow disaster affected five provinces, causing power line icing and supply disruptions that affected 3.83 million residents (Huang & Li, 2012). From 2010 to 2014, a total of 42 icing-related faults were recorded on 110 kV and above transmission lines in Hunan province alone (Xu & Cheng, 2017). Moreover, statistical analyses show that icing accounted for 5.1% of tripping events in 220 kV and above transmission lines in Zhejiang province during 2010–2020 (Zhou et al., 2021). These cases demonstrate that the power line icing is not only highly destructive but also has significant systemic impacts on the stability and reliability of regional power grids.

The mountainous regions of southwest Sichuan, China, are highly prone to severe power line icing due to the combined effects of complex topography and abundant atmospheric moisture (Tan et al., 1985; Wang, S., 1993; Wang, Z., 2011). This region is located in a plateau climate transition zone, bounded by the Tibetan Plateau to the west, the Yunnan-Guizhou Plateau to the south, the Sichuan Basin to the east, and the Qinling Mountains to the north (Xu et al., 2025). As a result of this unique geographical setting, the region is influenced by multiple large-scale climate systems, including the South Asian Monsoon and East Asian Monsoon (Xu et al., 2024; Zhang et al., 2019). The interaction between these climatic systems and complex terrain leads to pronounced spatial heterogeneity in power line icing, with locally severe icing conditions occurring frequently (Chai et al., 2023; Duan et al., 2018; Liu & Niu, 2015; Yan et al., 2009).

With the rapid development of power systems in China, an increasing number of ultra-high-voltage transmission lines traverse the mountainous regions of southwest Sichuan (Guo et al., 2019; Wang, Y. et al., 2022; Wang, H. et al., 2023). Owing to sparse regional icing observation and limited operational experience under icing conditions, the power infrastructure in this area faces considerable safety risks (Chai et al., 2023; Liu & Niu, 2015; Wang, Z., 2011). Given the increasing complexity of power grid structures and their critical role in supporting social and economic developments, accurately simulating or predicting transmission line icing processes is of great practical importance. Such simulations or predictions can supplement limited observations and improve the reliability of icing zone classification (Nygaard et al., 2013; Sokolov et al., 2025). Moreover, they enable real-time monitoring and forecasting of regional icing processes, facilitating timely mitigation measures during severe icing events (Hou et al., 2024; Musilek et al., 2009; Nygaard et al., 2017; Podolskiy et al., 2012). These capabilities enhance the resilience and proactive response of the power system to extreme icing conditions and help reduce the risk of icing-related failures (Chang et al., 2007; Hou et al., 2009; Weng et al., 2021). Overall, studies on power line icing simulation over the mountainous regions of southwest Sichuan provide important scientific support for the planning and safe operation of power transmission networks in China.

Various models have been developed to simulate power line icing, primarily falling into two categories: empirical and numerical approaches (Hou et al., 2024). Empirical models employ statistical methods to correlate icing events with meteorological variables, proving useful regional applications despite the limitation in accurate prediction of icing thickness (Cheng et al., 2022). In contrast, numerical models can describe the physical processes of ice accretion based on thermodynamic and fluid dynamic principles, achieving higher accuracy but requiring detailed input parameters that are often challenging to obtain through observations (Weng et al., 2021). Among these, the Makkonen model (Makkonen, 1989, 1998; Makkonen & Wichura, 2010) is the most widely adopted numerical framework and is recognized for its high predictive accuracy (Makkonen et al., 2018; Nygaard et al., 2011, 2013).

The application of the weather research and forecast (WRF) model has been shown to improve the accuracy of power line icing simulations (Podolskiy et al., 2012; Thompson et al., 2017). A commonly used methodology involves driving the Makkonen icing model with high-resolution meteorological variables produced by the WRF model to simulate the power line icing thickness (Nygaard et al., 2011; Sokolov et al., 2025). Among these input parameters, near-surface liquid water is particularly crucial, as it is largely influenced by the cloud microphysical scheme used in the WRF model (Nygaard et al., 2013, 2017). Previous studies (Gettelman & Morrison, 2015; Jones et al., 2018; Khain et al., 2015; Lim & Hong, 2010; Seiki et al., 2022) have demonstrated that the Thompson (Thompson et al., 2008) microphysical scheme provides a good balance between computational efficiency and operational applicability, whereas the Morrison scheme (Morrison et al., 2009) offers a more accurate representation of cloud microphysical processes. Furthermore, Nygaard et al. (2011) reported that the WRF model at a much higher horizontal resolution can lead to improved simulations of near-surface liquid water. However, existing studies on power line icing simulation focus on plains or general mountainous regions, with little systematic evaluation of the mountainous areas in southwest Sichuan. In this region, complex terrain and the interaction of multiple climate systems pose substantial challenges for high-quality meteorology simulations (Xu et al., 2024, 2025; Zhang et al., 2019). Consequently, the applicability and performance of the Makkonen model driven by WRF output in simulating power line icing under such conditions remain unclear.

To evaluate the performance of the WRF output-driven Makkonen model in simulating power line icing over the mountainous regions of southwest Sichuan, this study employed a four-level nested domain configuration to simulate eight observed icing events with horizontal resolutions of 9, 3, 1, and 0.33 km. The Thompson and Morrison cloud microphysical schemes were implemented separately. The effects of model resolution and cloud microphysical scheme on the accuracy of simulated icing thickness and near-surface meteorological conditions were systematically investigated. The results of this study may help address the scarcity of icing observations in the mountainous areas of southwest Sichuan and provide scientific support for the planning, construction, and safe operation of power transmission lines in this region.

The remainder of this paper is organized as follows. Section 2 describes the WRF and Makkonen models, cloud microphysical parameterizations, data sources, and research methodology. Section 3 evaluates the model performance in simulating the power line icing thickness and near-surface meteorological variables. Section 4 analyzes the underlying mechanism through which model resolution and cloud microphysical schemes influence the modeled icing processes and meteorological fields. Finally, Section 5 presents the conclusion and discussion.

2. Data and Methods

2.1. Data

The Sichuan Provincial Field Scientific Observation and Research Station for Power Infrastructure Icing and Safety at Erlangshan in the Plateau Transition Zone (hereafter referred to as Erlangshan station) is located on the southwestern margin of the Sichuan Basin, adjacent to the eastern edge of the Tibetan Plateau (Figures 1a–1d), at an elevation of 2987 m above sea level. From November to March, persistent orographic lifting frequently induces significant icing events. On average, around 30 icing events occur annually, with maximum icing thickness reaching about 90 mm during severe events (Xie & Wang, 2013). The station is equipped with three levels of LGJ-720/50 steel-core aluminum stranded conductors, each with a diameter of 36.2 mm (Figure 1e). The conductors are arranged along eat-west and north-south orientations, with a span length of 10 m, and are installed at heights of 2.2, 6.6, and 10 m above the ground surface. Additionally, the station includes a meteorological observation system that continuously monitors key atmospheric variables during icing events, including air temperature, dew point temperature, wet-bulb temperature, relative humidity, precipitation, air pressure, wind speed and direction, cloud cover and type, visibility, and weather phenomena (Figure 1e).

The air temperature and dew point temperature at 2 m height above ground surface observed at the Erlangshan station are employed to evaluate the performance of the WRF model in reproducing near-surface meteorological conditions. The air temperature characterizes the near-surface thermal environment, while the difference between air temperature and dew point temperature reflects the ambient humidity. Although wind speed is an important factor in icing accretion, the observational wind speed data are unreliable due to anemometer freezing. Therefore, the simulation accuracy of wind speed is not evaluated in this study. Meanwhile, all variables are measured four times per day at 02:00, 08:00, 14:00, and 20:00 BJT. The onset and end times of each icing event, along with the corresponding maximum icing thickness at 10 m height above ground surface, are incorporated into the experimental design and subsequently employed to validate the icing simulation results.

Moreover, the WRF model terrain information is provided by the Shuttle Radar Topography Mission (SRTM) 90 m digital elevation data (Jarvis et al., 2008), the model initial and lateral boundary conditions are derived from

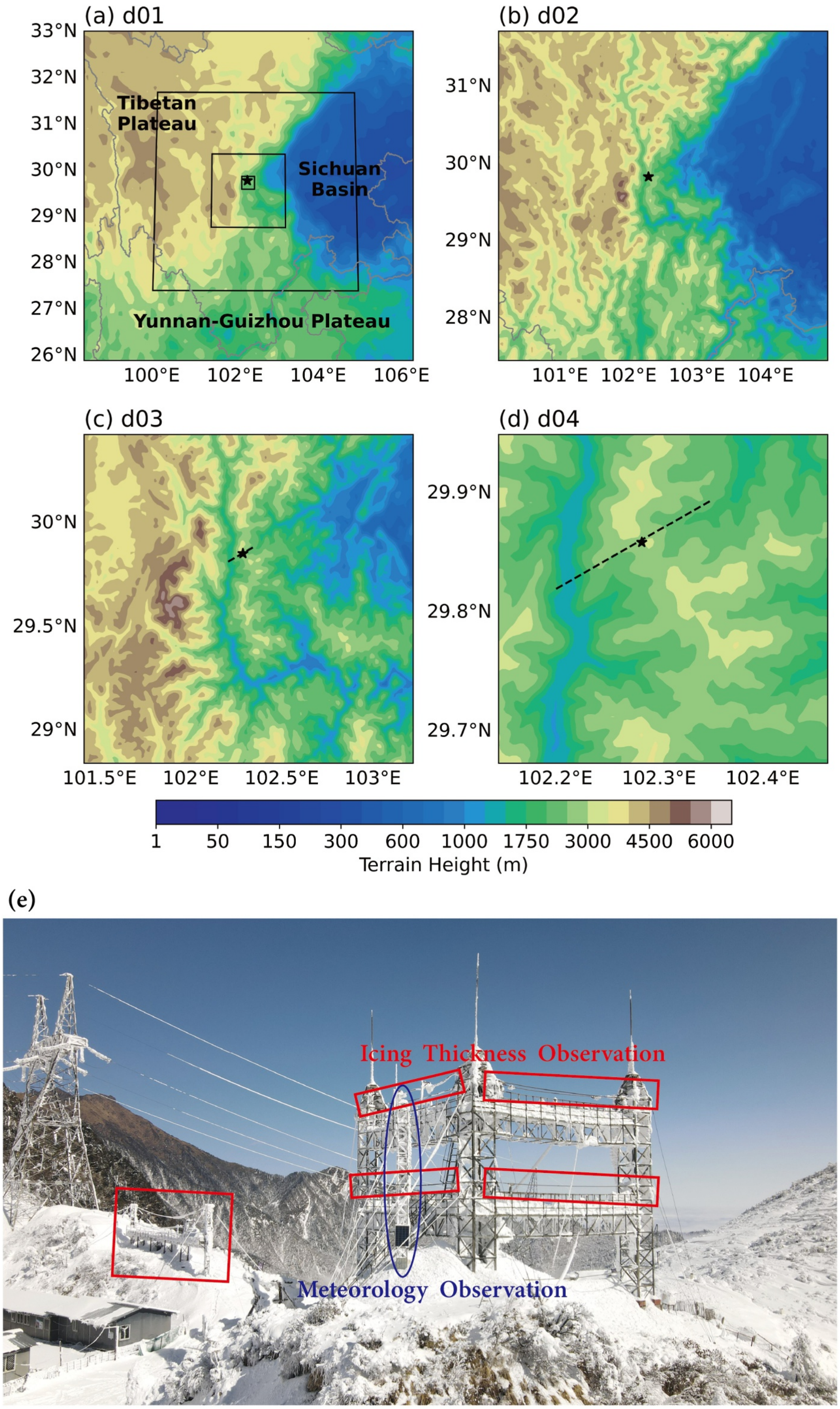

Figure 1. Terrain height (shaded) and the location of Erlangshan station (black star) within the four nested WRF domains (a–d). Panel (e) presents the Erlangshan station during the cold season. The gray lines in panels (a–b) denote the provincial administrative boundaries. Dashed lines in panels (c) and (d) indicate the approximate airflow pathway across the Erlangshan station.

the ERA5 global reanalysis with a time interval of 3 hr and a spatial resolution of 0.25° (Hersbach et al., 2020), and the monthly land cover information within each model grid is retrieved from the Moderate-resolution Imaging Spectroradiometer (MODIS) data with a horizontal resolution of 500 m (Friedl et al., 2010).

2.2. WRF and Makkonen Models

The WRF model version 4.2 is adopted in this study. It employs terrain-following vertical coordinates and supports multiple nesting strategies, allowing high-resolution simulations over regions with complex terrain while maintaining computational efficiency (Cai et al., 2025; Xu et al., 2024, 2025). The model includes a comprehensive suite of physical parameterization schemes, such as cloud microphysics, planetary boundary layer processes, radiation, surface layer physics, and land surface models, which can be flexibly configured to represent different atmospheric conditions (Zhang et al., 2025; Zhao et al., 2022). Its modular design enables users to tailor model configurations for specific research objectives. Owing to its high adaptability and strong community support, WRF has become one of the most widely used mesoscale atmospheric models worldwide, particularly for high-resolution simulations over complex terrain and extreme weather events (Cai et al., 2023; Zhang et al., 2019; Zhou et al., 2018).

The Makkonen model (Makkonen, 1989, 1998; Makkonen et al., 2018; Makkonen & Wichura, 2010) calculates power line icing thickness based on 3 physical processes: the collision, sticking, and freezing of supercooled liquid water onto the power line surface. It is expressed as

$$\frac{dM}{dt} = \eta_1 \cdot \eta_2 \cdot \eta_3 \cdot \mathrm{LWC} \cdot A \cdot v \tag{1}$$

where M is the mass of icing per unit length (kg·m^{-1}), t is the time interval (s), η_1 is the collision efficiency (unitless), η_2 is the sticking efficiency (unitless), η_3 is the freezing efficiency (unitless), LWC is the mass concentration of liquid water content (g·m^{-3}), A is the length of the power line cross-section (m), and v is the wind speed (m·s^{-1}) from the WRF output. LWC is calculated by the air pressure (P, hPa), air temperature (t_a, K), water vapor mixing ratio (QVAPOR, g·kg^{-1}), and cloud water mixing ratio (QCLOUD, g·kg^{-1}) from the WRF output as:

$$\rho_a = \frac{0.622 \cdot P \cdot (1 + \mathrm{QVAPOR})}{287 \cdot t_a \cdot (\mathrm{QVAPOR} + 0.622)} \tag{2}$$

$$\mathrm{LWC} = \mathrm{QCLOUD} \cdot \rho_a \tag{3}$$

where ρ_a is the air density (kg·m^{-3}).

The collision efficiency η_1 is less than 1, as small water droplets tend to follow the airflow and may be deflected away from the power line. The formula of η_1 is expressed as:

$$\eta_1 = A - 0.028 - C(B - 0.0454) \tag{4}$$

$$A = 1.066\mathrm{K}^{-0.00616} \times e^{-1.103\mathrm{K}^{-0.688}} \tag{5}$$

$$B = 3.641\mathrm{K}^{-0.498} \times e^{-1.497\mathrm{K}^{-0.694}} \tag{6}$$

$$C = 0.00637(\phi - 100)^{0.381} \tag{7}$$

$$K = \rho_w \cdot d^2 \cdot v / 9\mu \cdot D \tag{8}$$

$$\phi = R_e^2 / K \tag{9}$$

$$R_e = \rho_a \cdot d \cdot v / \mu \tag{10}$$

where $e = 2.718$ is a mathematical constant, $\rho_w = 1000$ is the water density (kg·m^{-3}), d is the water droplet diameter (m), $\mu = 1.7984 \times 10^{-5}$ is the absolute viscosity of air (kg·m^{-1} s^{-1}), D is the power line diameter (m), and R_e is the Reynolds number (unitless). d can be approximated using the median volume diameter (MVD), which is presented in the next section.

The formula of η_2 under wet-snow condition is developed empirically based on a combination of laboratory experiments and filed observations, and can be expressed as:

$$\begin{cases} \eta_2 = \frac{1}{v}, & v \geq 1\ \mathrm{m \cdot s^{-1}} \\ \eta_2 = 1, & v < 1\ \mathrm{m \cdot s^{-1}} \end{cases} \tag{11}$$

Liquid water droplets are typically assumed to have an sticking efficiency close to unity ($\eta_2 \approx 1$) because they rapidly freeze upon impact or spread over a wet surface without redounding, and any secondary splashing produces negligible mass loss.

Icing freezing generally occurs through two distinct regimes: dry growth and wet growth. Under dry growth conditions, all impinging super-cooled droplets freeze instantaneously upon contact with the surface, $\eta_3 = 1$. In contrast, during wet growth, only a portion of the captured droplets freezes immediately, while the remaining liquid may persist or refreeze after undergoing heat exchange processes at the ice surface. For wet growth conditions, the thermodynamic state of the ice surface is governed by an energy balance, which can be written as

$$Q_f + Q_v = Q_c + Q_e + Q_l + Q_s \tag{12}$$

This equation accounts for multiple heat flux components, including: the latent heat released by freezing (Q_f), aerodynamic heating (Q_v), sensible heat exchange with the surrounding air (Q_c), evaporative cooling (Q_e), heat exchange associated with warming or cooling of incoming droplets to the freezing point (Q_l), and radiative heat transfer (Q_s). Each term in the surface energy balance can be parameterized using meteorological variables and structural characteristics of the freezing object as described in Equations 13–18.

$$Q_f = (1-\lambda) \cdot \eta_3 \cdot F \cdot L_f \tag{13}$$

$$Q_v = \frac{h \cdot r \cdot v^2}{2C_p} \tag{14}$$

$$Q_c = h \cdot (t_s - t_a) \tag{15}$$

$$Q_e = \frac{h \cdot \varepsilon \cdot L_e . (e_s - e_a)}{C_p . P} \tag{16}$$

$$Q_l = F \cdot C_W \cdot (t_s - t_d) \tag{17}$$

$$Q_s = \sigma \cdot a \cdot (t_s - t_d) \tag{18}$$

where $\lambda = 0.26$ is the liquid fraction of the accretion (unitless), $F = \eta_1 \cdot \eta_2 \cdot \mathrm{LWC} \cdot v$ is the flux density of water to surface ($\mathrm{g \cdot m^{-2}\, s^{-1}}$), $L_f = 3.34 \times 10^5$ is the latent heat of water ($\mathrm{J \cdot kg^{-1}\, K^{-1}}$), h is the convective heat transfer coefficient (unitless), $r = 0.79$ is the recovery factor for viscous heating (unitless), $C_p = 1004.07$ is the specific heat of air ($\mathrm{J \cdot kg^{-1}\, K^{-1}}$), t_s is the temperature of the icing surface (K), $\varepsilon = 0.62$ is the ratio of the molecular of dry air and water vapor (unitless), $L_e = 2.501 \times 10^6$ is the latent heat of vaporization ($\mathrm{J \cdot kg^{-1}\, K^{-1}}$), e_s is the saturation water vapor pressure over the accretion surface (hPa), e_a is the ambient vapor pressure in the air stream (hPa), P is the air pressure (hPa), $C_W = 4218$ is the specific heat of water ($\mathrm{J \cdot kg^{-1}\, K^{-1}}$), t_d is the temperature of the droplets at impact (K), $\sigma = 5.67 \times 10^{-8}$ is the Stefan-Boltzmann constant ($\mathrm{W \cdot m^{-2}\, K^{-4}}$), and $a = 8.1 \times 10^7$ is radiation linearization constant (K^3). Based on the above formulations, η_3 can ultimately be expressed as:

$$\eta_3 = \frac{h}{F \cdot (1-\lambda) \cdot L_f}\left[(t_s - t_a) + \frac{\varepsilon \cdot L_e}{C_P \cdot P}(e_s - e_a) - \frac{r \cdot v^2}{2C_P}\right] + \frac{C_W \cdot (t_s - t_d)}{(1-\lambda) \cdot L_f} + \frac{\sigma \cdot a \cdot (t_s - t_a)}{F \cdot (1-\lambda) \cdot L_f} \tag{19}$$

Using the above formulation, the icing mass accumulation can be calculated at each time step for every model grid. Assuming the icing density is 900 kg·m^{-3} and that the accreted ice forms a standard cylindrical shape around the conductor, the corresponding icing thickness (H) can be derived by $H = \sqrt{M/900/\pi} - D/2$.

2.3. Cloud Microphysical Parameterizations

Thompson et al. (2008) represents the cloud water droplets size (D_p) distribution using a generalized Gamma distribution:

$$N(D_p) = N_0 \cdot D_p^{\beta} \cdot e^{-\lambda D_p} \tag{20}$$

where N_0, λ, and β are the intercept, slope, and shape parameters, respectively. Those parameters are diagnosed as

$$\beta = \min\left(15, \frac{1000}{N_c} + 2\right) \tag{21}$$

$$N_0 = \frac{N \cdot \lambda^{\beta+1}}{\Gamma(\beta+1)} \tag{22}$$

$$\lambda = \left[\frac{\pi}{6} \cdot \rho_w \cdot \frac{\Gamma(\beta+4)}{\Gamma(\beta+1)} \cdot \left(\frac{N_c}{\mathrm{LWC}}\right)\right]^{1/3} \tag{23}$$

where N_c is the total droplet number concentration (cm^{-3}). Consequently, MVD can be obtained from Equation 24:

$$\mathrm{MVD} = \frac{3.672 + \beta}{\lambda} \tag{24}$$

Thompson et al. (2008) assume a fixed total droplet number concentration of 250 cm^{-3} for continental regions, which yields $\mathrm{MVD} = 21.25 \cdot \mathrm{LWC}^{1/3}$.

In contrast, Morrison et al. (2009) first converted the cloud droplet number concentration mixing ratio to a volumetric concentration using air density. The shape parameter is then diagnosed empirically as

$$\beta = \mathrm{clip}\left(\frac{1}{\left[0.0005714 \cdot \frac{N}{10^6} \cdot \rho_a + 0.2714\right]^2} - 1, 2, 10\right) \tag{25}$$

After β is determined, λ is calculated by:

$$\lambda = \left[\frac{\pi}{6} \cdot \rho_w \cdot \frac{\Gamma(\beta+4)}{\Gamma(\beta+1)} \cdot \left(\frac{N}{\mathrm{QCLOUD}}\right)\right]^{1/3} \tag{26}$$

MVD is subsequently obtained from the incomplete Gamma-function relationship:

$$\gamma(\beta+4, \lambda \cdot \mathrm{MVD}) = \frac{1}{2}\Gamma(\beta+4) \tag{27}$$

Assuming N is fixed at 250 cm^{-3} and $\rho_a = 1.225$ kg·m^{-3} yields $\beta \approx 4.02$. And then by applying Equations 23 and 24 gives an approximate formula for $\mathrm{MVD} = 21.79 \cdot \mathrm{LWC}^{1/3}$.

Table 1
Observation and Simulation Periods for the Eight Icing Events at the Erlangshan Station

Event	Observation period (BJT)	Simulation period (BJT)
Event 1	From 2024-12-04 08:00 to 2024-12-08 13:35	From 2024-12-03 20:00 to 2024-12-09 00:00
Event 2	From 2024-12-11 17:10 to 2024-12-15 11:05	From 2024-12-11 05:00 to 2024-12-16 00:00
Event 3	From 2024-12-19 19:10 to 2024-12-22 12:50	From 2024-12-19 05:00 to 2024-12-23 00:00
Event 4	From 2025-01-06 18:50 to 2025-01-10 15:50	From 2025-01-06 05:00 to 2025-01-11 00:00
Event 5	From 2025-01-23 17:25 to 2025-01-26 16:15	From 2025-01-23 05:00 to 2025-01-27 00:00
Event 6	From 2025-01-30 14:15 to 2025-02-01 13:20	From 2025-01-30 02:00 to 2025-02-02 00:00
Event 7	From 2025-02-04 15:20 to 2025-02-07 15:30	From 2025-02-04 02:00 to 2025-02-08 00:00
Event 8	From 2025-02-11 15:35 to 2025-02-13 10:50	From 2025-02-11 02:00 to 2025-02-14 00:00

2.4. Experimental Design

This study designs two numerical experiments conducted by the WRF model, adopting the Thompson (Thompson et al., 2008) and Morrison (Morrison et al., 2009) cloud microphysical schemes, separately. Both experiments are carried out with the same model configuration. The only difference between the two experiments lies in the distinct cloud microphysical schemes employed. The simulation area is centered at 29.53°N, 102.32°E with four one-way nested domains (Figure 1). The model horizontal resolution (integration time step) of the four domains increases by a factor of 3 from 9 km (18 s) in the outermost domain to 0.33 km (0.67 s) in the innermost domain, with the model grids (meridian × parallel) of 90 × 90, 160 × 160, 178 × 178, 94 × 94, respectively. The innermost domain (d04) is configured with a relatively small number of grid points to focus computational resources on the target area. And limiting the domain size helps maintain numerical stability during model integration at very high resolution over complex terrain regions. The four domains all run with 50 vertical levels of atmosphere with 50 hPa at the model top.

According to previous studies (Cai et al., 2023; Ma et al., 2022; Nygaard et al., 2011; Xu et al., 2025) and extensive numerical experiments, the following schemes are adopted for the model integration: the CAM3 short-wave and long-wave radiation schemes (Collins et al., 2004), the Eta similarity surface layer scheme (Janjić, 1994), the Noah Land Surface Model (Chen & Dudhia, 2001), and the MYJ planetary boundary layer scheme (Janjić, 1994). Convection is assumed to be explicitly resolved in the inner 3 domains. Thus, the Grell-Freitas cumulus scheme (Grell & Freitas, 2014) is implemented in the outermost domain, but no cumulus scheme is applied in the inner 3 domains. The model output frequency is set to 1 hr.

Based on the above model configuration, this study reproduces eight icing events in Erlangshan station by adopting the WRF and Makkonen models. Table 1 gives the observation and simulation periods for the eight events. Each simulation ensures at least 12 hr for the model spin-up. From Table 1, it is evident that the icing events at Erlangshan station tend to occur in the late afternoon and conclude around noon. Otherwise, the icing process typically lasts 3 to 4 days.

The meteorological data from the first vertical layer of the WRF output drives the Makkonen model for calculating the icing thickness. A grid cell is identified as experiencing icing when the following meteorological criteria are simultaneously met: (a) air temperature is between −13°C and 3°C, (b) relative humidity exceeds 85%, and (c) the mass concentration of water content is greater than 0.07 $g \cdot m^{-3}$.

Once these conditions are satisfied, the Makkonen model computes the hourly collision and freezing efficiencies and icing accumulation at each grid point. This is achieved by integrating meteorological conditions from the WRF output based on Equations 1–19. The process iterates until the event concludes, with the final outputs including the temporally averaged collision efficiency, freezing efficiency, and the maximum icing thickness.

2.5. Metrics

This study adopts the inverse distance weighting method (Bartier & Keller, 1996; Huang et al., 2016; Luo et al., 2025) to interpolate data from the 12 nearest model grid points to the observation station. The interpolated results are then evaluated using the root mean square error (RMSE) to quantify the absolute error and the Taylor

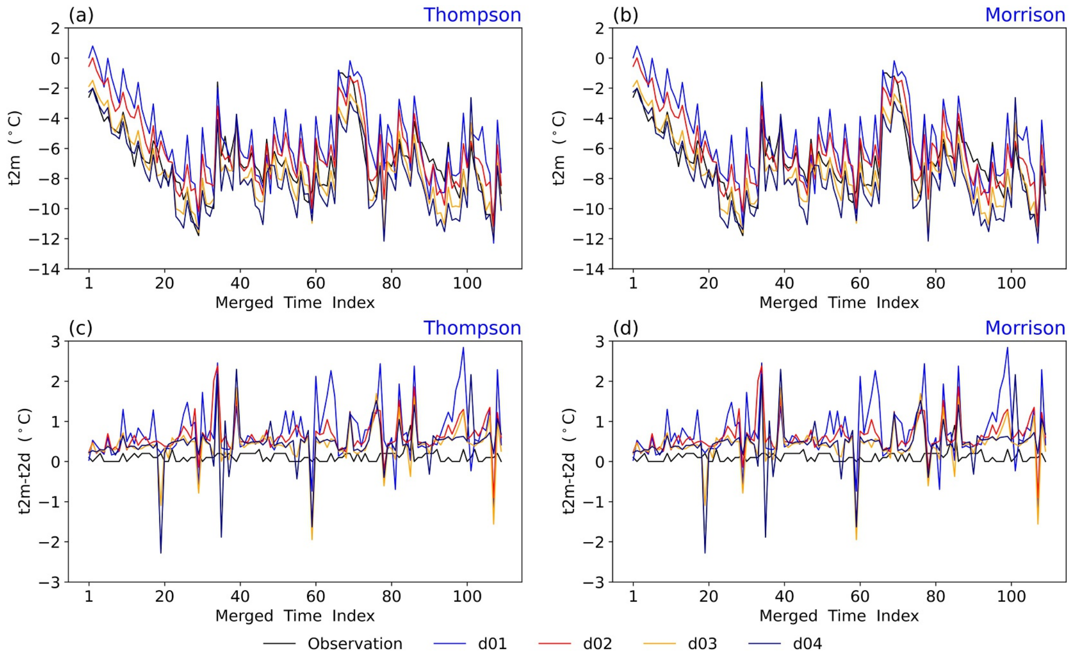

Figure 2. Comparison of observed and WRF simulated time series of near-surface air temperature (t2m; panels a–b) and the temperature-dew point difference (t2m-t2d; panels c–d) at Erlangshan station during the eight icing events, under different horizontal resolutions and cloud microphysical schemes. The time axis represents a merged time index of all events, with each point corresponding to matched observation times.

score (TS) to assess the temporal consistency between the simulation and observation (Huang et al., 2019; Luo et al., 2023; Zhang et al., 2024). The formula of TS is expressed as

$$\mathrm{TS} = \frac{4(1+R)}{\left(\sigma+\frac{1}{\sigma}\right)^2(1+R_0)} \tag{28}$$

$$R = \frac{\sum_{i=1}^{N}(x_i-\overline{x})\left(y_i-\overline{y}\right)}{\sqrt{\sum_{i=1}^{N}(x_i-\overline{x})^2}\sqrt{\sum_{i=1}^{N}\left(y_i-\overline{y}\right)^2}} \tag{29}$$

$$\sigma = \frac{\sqrt{\frac{1}{N}\sum_{i=1}^{N}(x_i-\overline{x})^2}}{\sqrt{\frac{1}{N}\sum_{i=1}^{N}\left(y_i-\overline{y}\right)^2}} \tag{30}$$

where x_i and y_i denote the simulated and observed values at the ith time step, respectively, for a total of N samples. Their corresponding temporal means are given by $\overline{x}$ and $\overline{y}$. R indicates the correlation coefficient between the simulations and observations, while σ quantifies their standard deviation. $R_0 = 1$ represents the theoretical upper limit of the correlation that can be achieved.

3. Results

Near-surface meteorological conditions control the occurrence and duration of power line icing. Figure 2 presents the comparison between simulated and observed time series of 2 m air temperature and the difference between air temperature and dew point temperature at Erlangshan station during the eight icing events. Overall, the 2 m air temperature ranges from −12°C to 2°C and exhibits distinct diurnal and seasonal variability, whereas the difference between air temperature and dew point temperature remains relatively stable within ±2°C. The WRF simulations using both the Thompson and Morrison schemes broadly reproduce similar temporal evolution of near-surface meteorological conditions. As the model's horizontal resolution increases, the simulated near-surface thermal and moisture fields show progressively better agreement with the observations.

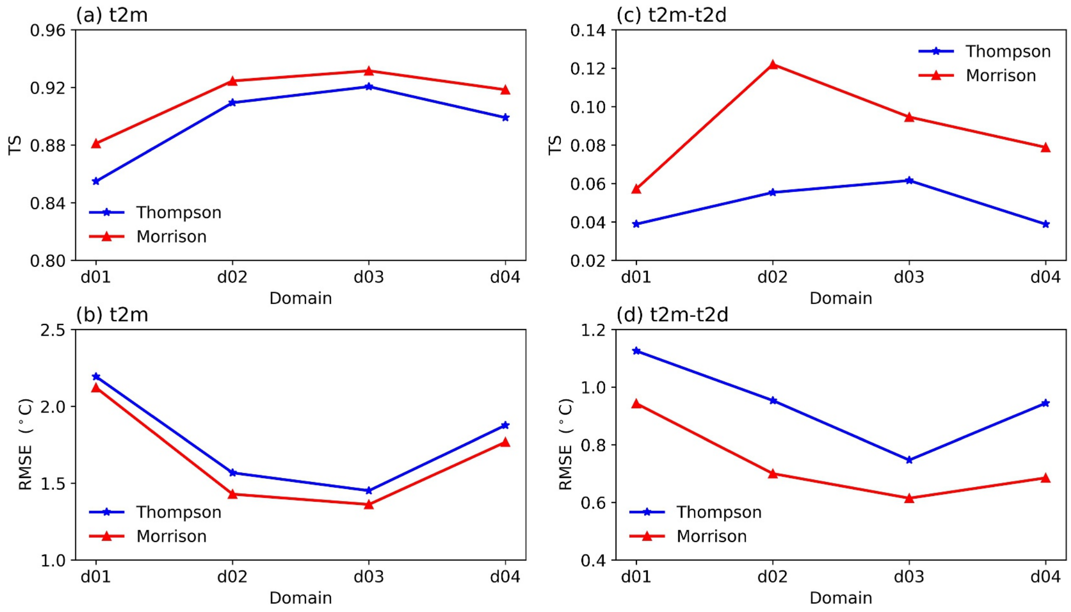

Figure 3. The TS and RMSE for the near-surface air temperature (t2m; panels a–b) and the temperature-dew point difference (t2m-t2d; panels c–d) simulated by the WRF model under different horizontal resolutions and cloud microphysical schemes during the eight icing events at Erlangshan station. The statistics are calculated based on the concatenated time series from all eight icing events.

Figure 3 shows the RMSE and TS of the simulated near-surface thermal and moisture variables relative to the observations. Apparently, the WRF model demonstrates higher skill in representing near-surface thermal conditions than moisture conditions. The TS (RMSE) values for simulated 2 m air temperature range from 0.84 to 0.93 (from 1.40°C to 2.20°C), while those for the air temperature-dew point temperature difference range from 0.03 to 0.13 (from 0.60°C to 1.10°C). Among the four horizontal resolutions, the 1 km configuration exhibits the best overall performance in simulating near-surface thermal and moisture conditions at Erlangshan station, as indicated by the lowest RMSE and highest TS. Additionally, the Morrison scheme outperforms the Thompson scheme in near-surface thermal and moisture simulations at Erlangshan station, with TS values approximately 0.02 higher and RMSE values about 0.1°C lower under all horizontal resolutions.

As shown in Figure 4, the simulation accuracy of near-surface thermal and moisture conditions at the Erlangshan station varies substantially among the eight icing events, indicating that the model performance is sensitive to differences in synoptic background and local terrain-induced processes. Nevertheless, a clear improvement is evident with increasing horizontal resolution. Both the RMSE and TS boxplots show that the simulations at 1 km resolution provide the most accurate representation of near-surface thermal and moisture conditions, with lower median RMSE values and higher TS values. Additionally, the simulations using the Morrison microphysical scheme consistently outperform those using the Thompson microphysical scheme. The Morrison scheme generally yields lower RMSE and higher TS values, indicating a more accurate representation of the near-surface thermodynamic environment. Moreover, the inter-event spread of both metrics is smaller for the Morrison scheme, suggesting that it provides a more stable and robust performance across different icing events. Overall, the WRF configuration employing the Morrison scheme with a horizontal resolution of 1 km provides the most accurate simulation of near-surface meteorological conditions at the Erlangshan station.

As illustrated in Figure 5, the simulated icing thickness averaged by eight icing events is predominantly distributed along the periphery of the Sichuan Basin, extending southward from its western boundary adjacent to the Tibetan Plateau to its southern boundary bordering the Yunnan-Guizhou Plateau. The icing thickness reaches approximately 20 mm in the transition zone between the Sichuan Basin and the Tibetan Plateau, whereas it exceeds 30 mm at the interface between the Sichuan Basin and the Yunnan-Guizhou Plateau. This spatial pattern is largely governed by the combined influences of atmospheric water vapor transport and orographic lifting. The southern and western boundaries of the Sichuan Basin provide major routes for atmospheric water vapor influx, with the southern transport pathway exerting the dominant influence on precipitation formation within and around

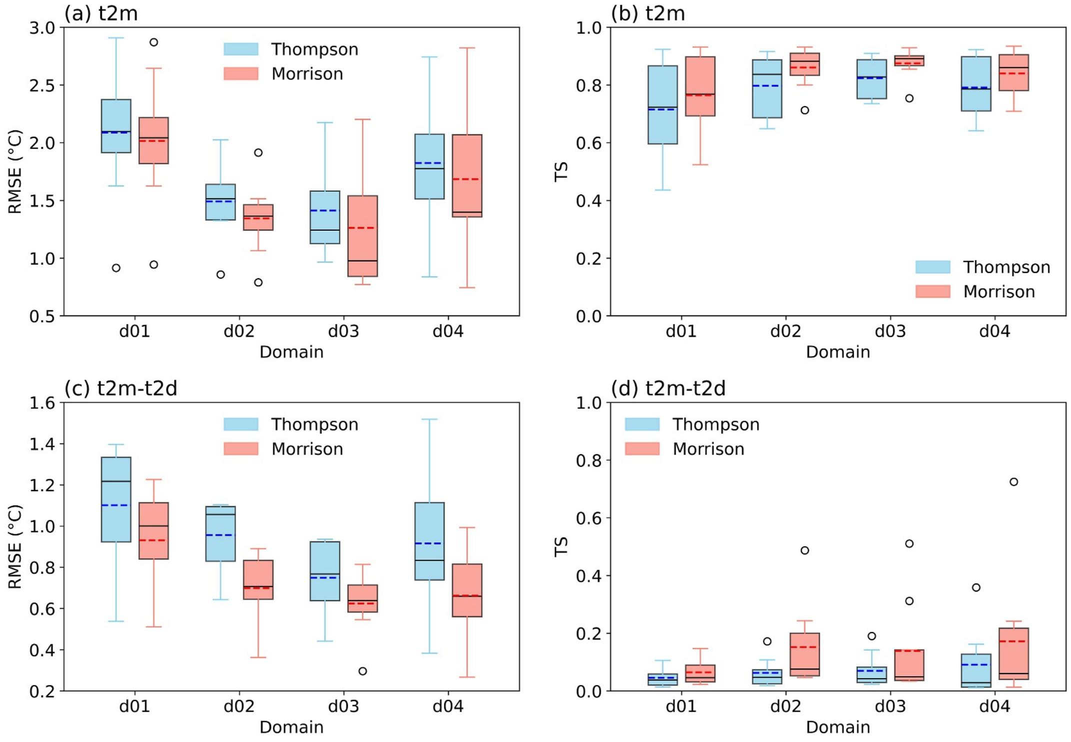

Figure 4. Box-and-whisker plots showing the distribution of (a) RMSE and (b) TS for near-surface air temperature (t2m), and (c) RMSE and (d) TS for the temperature-dew point difference (t2m-t2d) across the eight icing events for the four nested domains. For each event, RMSE and TS are calculated individually, and the resulting eight values are used to construct the box plots. Results obtained using the Thompson and Morrison cloud microphysical schemes are presented side by side for each domain.

the basin (Xu et al., 2024; Zhang et al., 2019). Notably, as the model spatial resolution increases, micro-topographic features become more evident in the simulated icing thickness. In domains d03 and d04, the spatial distribution of icing thickness closely corresponds to the underlying terrain. Additionally, the overall spatial characteristics of icing thickness are generally consistent across the different cloud microphysical schemes. However, as shown in Figures 5i–5l, the simulations by adopting the Morrison cloud scheme typically produce icing thickness values up to 10 mm greater than those generated by adopting the Thompson cloud scheme in all the four domains.

Figure 6 presents a comparison between the simulated and observed icing thicknesses at the Erlangshan station. All eight icing events are characterized by substantial icing, with observed icing thicknesses exceeding 30 mm, and the most severe event with the icing thickness of 55.20 mm (Figures 6a and 6b). Overall, the simulated icing thicknesses are systematically underestimated with the mean biases ranging from 0.90 mm to −48.70 mm (Figures 6c and 6d). This negative bias is likely attributable to two primary factors. First, limitations in terrain representation within the WRF model may lead to an underestimation of wind speed amplification associated with the mountain pass terrain at Erlangshan station (Figure 1e). Second, additional uncertainties arise from the icing accretion process in the Makkonen model, which may further contribute to the underestimation of icing thickness. Notably, although increasing the model horizontal resolution does not always lead to smaller mean bias in simulated icing thickness for every icing event (Figures 6c and 6d), the overall simulation error decreases systematically as the horizontal resolution increases. As shown in Figure 6e, the RMSE of the icing thickness simulation is substantially reduced at a finer resolution. For simulations adopting the Thompson scheme, the RMSE decreases from 40.67 to 24.16 mm as the horizontal resolution increases from 9 to 0.33 km. An even larger reduction is obtained when the Morrison scheme is used, with the RMSE decreasing from 37.47 to 14.44 mm. The simulated icing thickness is also sensitive to the choice of cloud microphysical scheme. The icing thicknesses simulated by the Makkonen model driven by the output of the WRF model using the Morrison microphysical scheme exhibit much better agreement with observations than those using the Thompson scheme (Figure 6e).

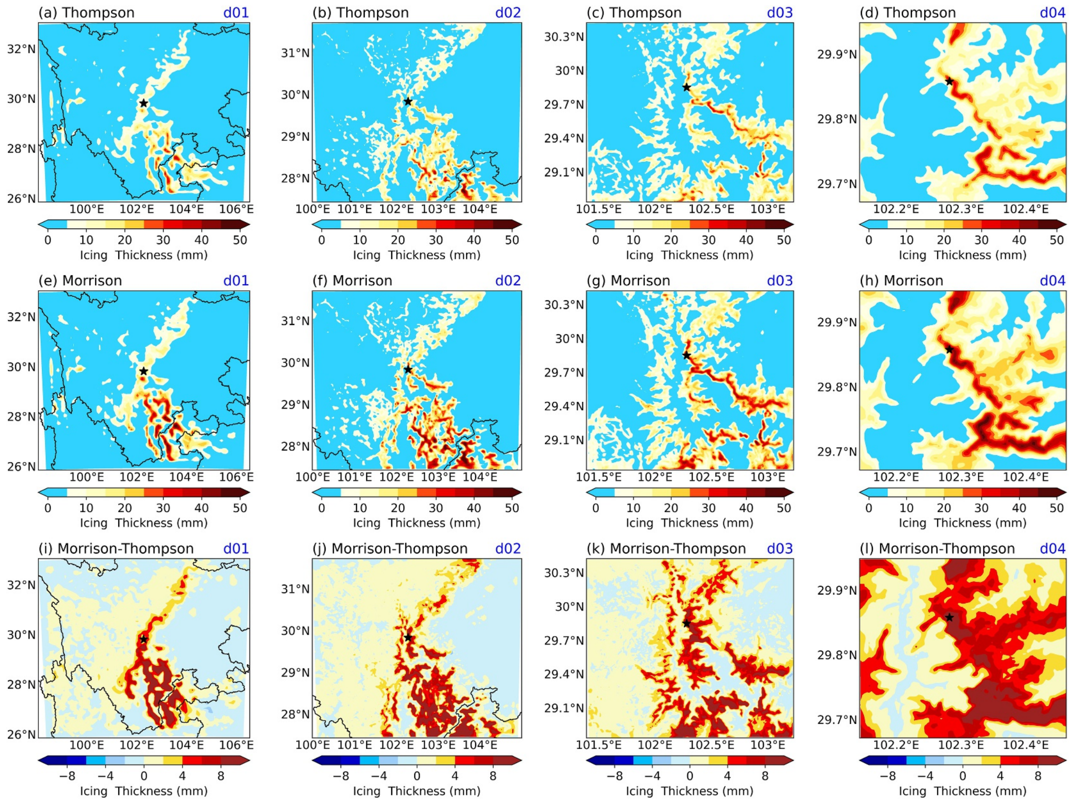

Figure 5. The spatial distribution of mean simulated icing thickness among the eight icing events in four WRF domains adopting the Thompson (a–d) or Morrison (e–h) cloud microphysical scheme, and their differences (i–l). The black lines indicate the provincial administrative boundaries, and the black stars represent the location of Erlangshan station.

Across the different horizontal resolutions, the RMSE of icing thickness obtained using the Morrison scheme is 3.20–10.42 mm lower than that obtained using the Thompson scheme.

4. Possible Mechanisms

Figure 7 illustrates that the spatial patterns of the differences in near-surface air temperature, wind speed, cloud water, liquid water content, collision efficiency, and freezing efficiency retrieved from the WRF output between adopting the Morrison and Thompson microphysical schemes in domain d04 are broadly consistent with that of the icing thickness differences. In domain d04, the WRF model adopting the Morrison scheme produces slightly lower air temperature (~0.10°C), higher wind speed (~0.10 $m\cdot s^{-1}$), and enhanced cloud water (up to 0.12 $g\cdot kg^{-1}$) compared to using the Thompson scheme. This further leads to higher liquid water content (up to 0.15 $g\cdot m^{-3}$) as well as increased collision efficiency (up to 0.35) and freezing efficiency (up to 0.30). The spatial correlation analysis shows that the liquid water content, collision efficiency, and freezing efficiency are positively correlated with the icing thickness, whereas air temperature and wind speed exhibit negative correlations. All spatial correlation coefficients (SCC) pass the 99% confidence level based on the Student's t-test, indicating robust relationships. Among those factors, liquid water content shows the strongest correlation with icing thickness (SCC = 0.91), followed by collision efficiency (SCC = 0.72) and freezing efficiency (SCC = 0.55), while wind speed (SCC = −0.30) and air temperature (SCC = −0.20) display relatively weaker correlations.

Physically, the icing process is governed by the collision and subsequent freezing of super-cooled droplets on conductor surfaces (Equations 1–19). Liquid water content provides the fundamental source of super-cooled droplets and thus exerts the primary control on icing accumulation. Otherwise, collision and freezing efficiencies regulate the growth rate of icing, explaining their relatively strong correlations with icing thickness. Notably, the icing process in the study area is dominated by a dry-growth condition in which the freezing efficiency is close to unity and exhibits limited variability (figure not shown), thereby reducing its relative

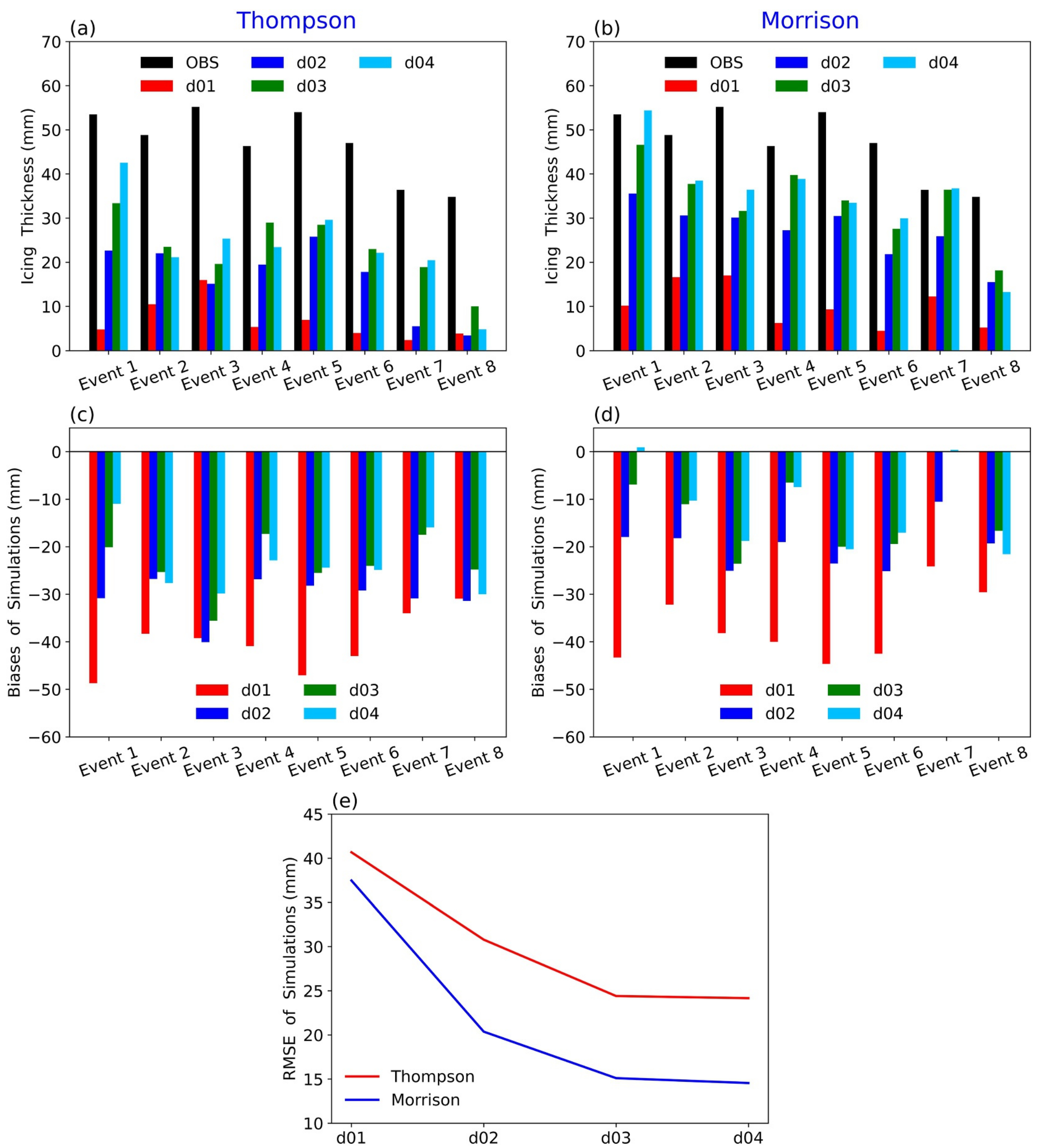

Figure 6. Comparison between the observed (OBS) and simulated icing thicknesses in domains d01-d04 using the Thompson (a) or Morrison (b) cloud microphysical schemes for the eight icing events. Panels (c) and (d) present corresponding biases of the simulated icing thicknesses relative to the observations, while panel (e) shows the RMSE.

contribution compared with the collision efficiency. Moreover, wind speed plays a dual role (Makkonen et al., 2018; Nygaard et al., 2011; Podolskiy et al., 2012; Sokolov et al., 2025): insufficient wind limits droplet impingement, while excessive wind deflects airflow away from the conductor or even promotes ice shedding, leading to an overall negative correlation with icing thickness. In contrast, icing predominantly occurs under persistently low-temperature conditions in winter, and the complex terrain of Erlangshan maintains a sufficiently cold environment such that small air temperature variations exert only a minor influence on icing variability.

As shown in Figure 8, the spatial distribution of atmospheric liquid water is strongly controlled by terrain-induced lifting. Liquid water is primarily concentrated between 2500 and 3,500 m (approximately within 1 km above ground level) on the windward slope of Erlangshan station, with values reaching ~0.20 g·m^{-3} (Figures 8a–8d). This magnitude is generally consistent with observations reported in previous studies (Sokolov et al., 2025; Yuan et al., 2025). With increasing horizontal resolution, the terrain becomes more realistically represented, leading to enhanced orographic lifting and a more pronounced accumulation of liquid water near the ridge in domain d04.

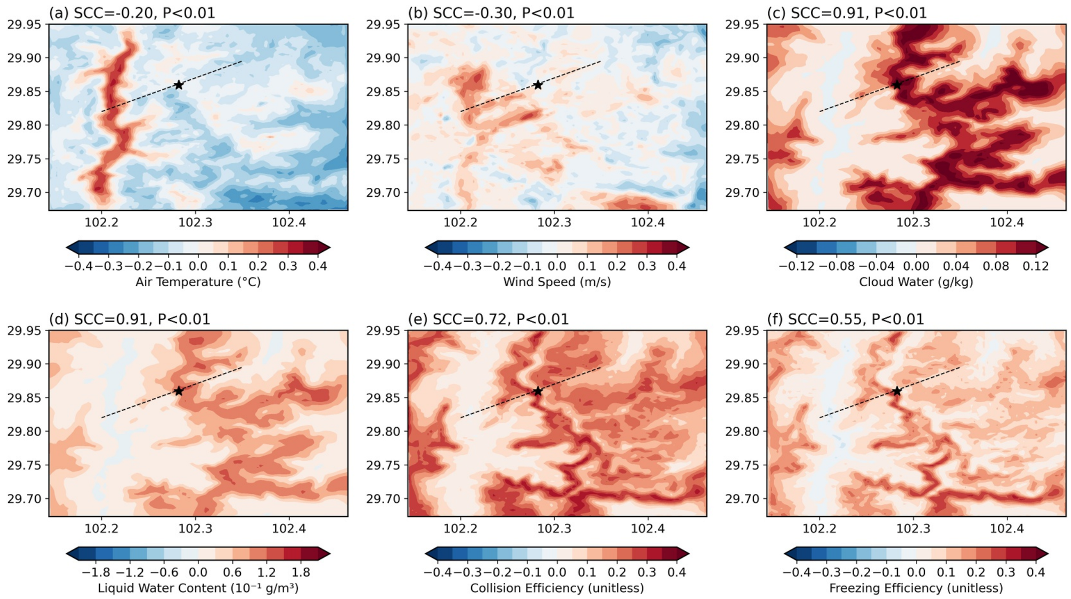

Figure 7. Same as Figure 5l, but for the near-surface air temperature (a), wind speed (b), cloud water (c), liquid water content (d), collision efficiency (e), and freezing efficiency (f) from the WRF output. The former three are directly output by the model, whereas the latter three are diagnosed from the WRF simulated fields. The value of SCC in each panel denotes the spatial correlation coefficient between the corresponding variable difference and the difference in icing thickness (Figure 5l), and all correlations are significant at the 99% confidence level according to the Student's *t*-test. The dashed line indicates the approximate airflow pathway across the Erlangshan station.

Compared to the Thompson scheme, the WRF model using the Morrison scheme produces a noticeable increase in liquid water, particularly near the windward ridge, with differences reaching up to ~0.12 $g{\cdot}m^{-3}$ (Figures 8e and 8f). However, this increase is not accompanied by stronger dynamical conditions. The along-flow wind speed even shows a slight decrease, and the vertical velocity is also marginally weakened (<1 $m{\cdot}s^{-1}$). These results suggest that the enhanced liquid water content in simulations adopting the Morrison scheme is unlikely to be caused by increased moisture transport or stronger orographic uplift.

Figure 9 further reveals that the simulation differences in liquid water content originate from microphysical processes. In domain d04, the WRF model using the Morrison scheme produces substantially higher cloud water mixing ratios, especially over the windward ridge, with increases up to ~0.12 $g{\cdot}kg^{-1}$ (Figure 9a). Although rainwater also increases on the windward slope, its magnitude is much smaller (on the order of $0.04\text{–}0.32 \times 10^{-2}$ $g{\cdot}kg^{-1}$, Figure 9b). In contrast, the solid-phase hydrometeors show a slight decrease over most regions (~0.32×10^{-2} $g{\cdot}kg^{-1}$, Figure 9c). Meanwhile, the rain number concentration increases significantly by up to ~9,000 kg^{-1} (Figure 9d), indicating a shift of the particle size distribution toward smaller droplets. This shift implies reduced efficiency of autoconversion and accretion, thereby limiting the conversion of cloud water into cloud rain. Consistent with this interpretation, Morrison et al. (2009) demonstrated that this scheme tends to suppress in-cloud evaporation and enhance stratiform precipitation, which is also associated with a shift of the particle size distribution toward smaller droplets. In addition, the reduction in solid hydrometeors suggests a weakening of ice-phase processes, which further decreases the consumption of liquid water.

Taken together, these results indicate that the increased cloud water in the WRF output using the Morrison scheme relative to the Thompson scheme is primarily driven by changes in cloud microphysical processes rather than dynamic effects. Specifically, the increase in droplet number concentration and the shift toward smaller particle sizes reduce the efficiency of liquid-to-precipitation and liquid-to-ice conversion pathways. As a result, more condensate is retained in the liquid phase. This enhanced reservoir of super-cooled liquid water provides a more available mass for collision and freezing processes, ultimately leading to a larger simulated icing thickness.

From Figure 10, the enhanced terrain detail better captures the cooling effect over the ridge (Figure 10a) and the acceleration of near-surface wind speed (Figure 10b). These dynamical features favor higher collision efficiency (Figure 10c) and freezing efficiency (Figure 10d) of super-cooled droplets on the conductor surface, thereby

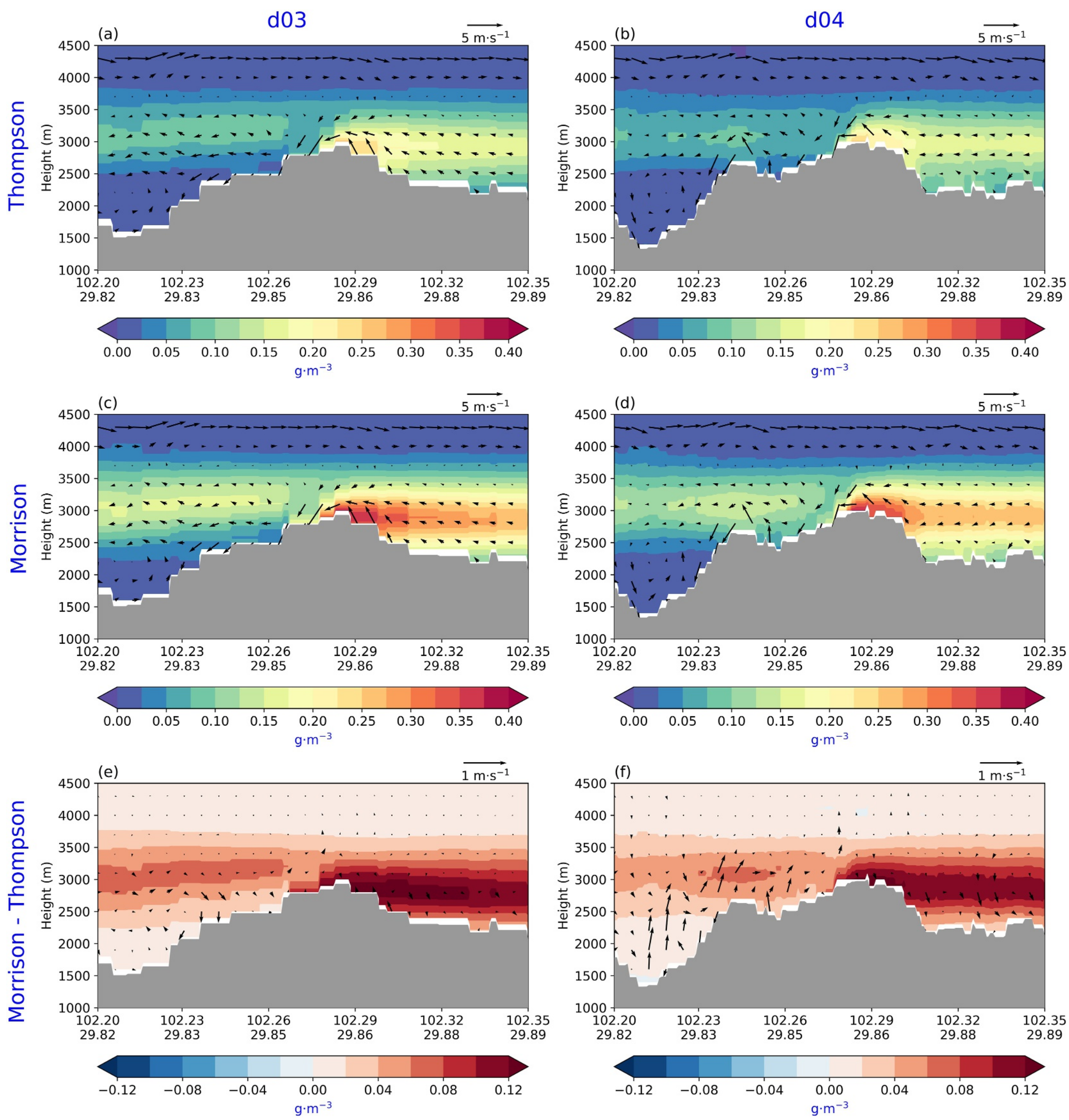

Figure 8. Time-mean cross sections of liquid water content (shading) and wind speed (vector) along the airflow pathway shown in Figure 7, averaged over the eight icing events. Gray shading denotes the underlying terrain. Panels (a) and (b) show the results simulated using the Thompson scheme for domains d03 and d04, respectively; panels (c) and (d) show the corresponding results simulated using the Morrison scheme; panels (e) and (f) show the corresponding differences between the two schemes (Morrison-Thompson), respectively.

providing more favorable conditions for icing formation. Additionally, the differences between adopting the Morrison and Thompson schemes in simulated near-surface air temperature and wind speed are relatively small, with no substantial enhancement in dynamical forcing in simulations adopting the Morrison scheme (Figures 10a and 10b). However, despite the limited dynamical differences, the WRF model using the Morrison scheme produces higher collision and freezing efficiencies along the ridge (Figures 10c and 10d). This is mainly attributed to the increased liquid water content (Figures 8e and 8f), which provides a larger reservoir of super-cooled droplets available for collision and freezing.

Overall, increasing the model horizontal resolution leads to a more realistic representation of terrain complexity, which enhances the simulated cooling effect, wind acceleration, and orographic lifting along the ridge. These dynamical improvements promote the formation of super-cooled liquid water and increase both collision and freezing efficiencies, ultimately resulting in a larger simulated icing thickness. Moreover, the WRF model adopting the Morrison cloud microphysical scheme modifies the particle size distribution by increasing the

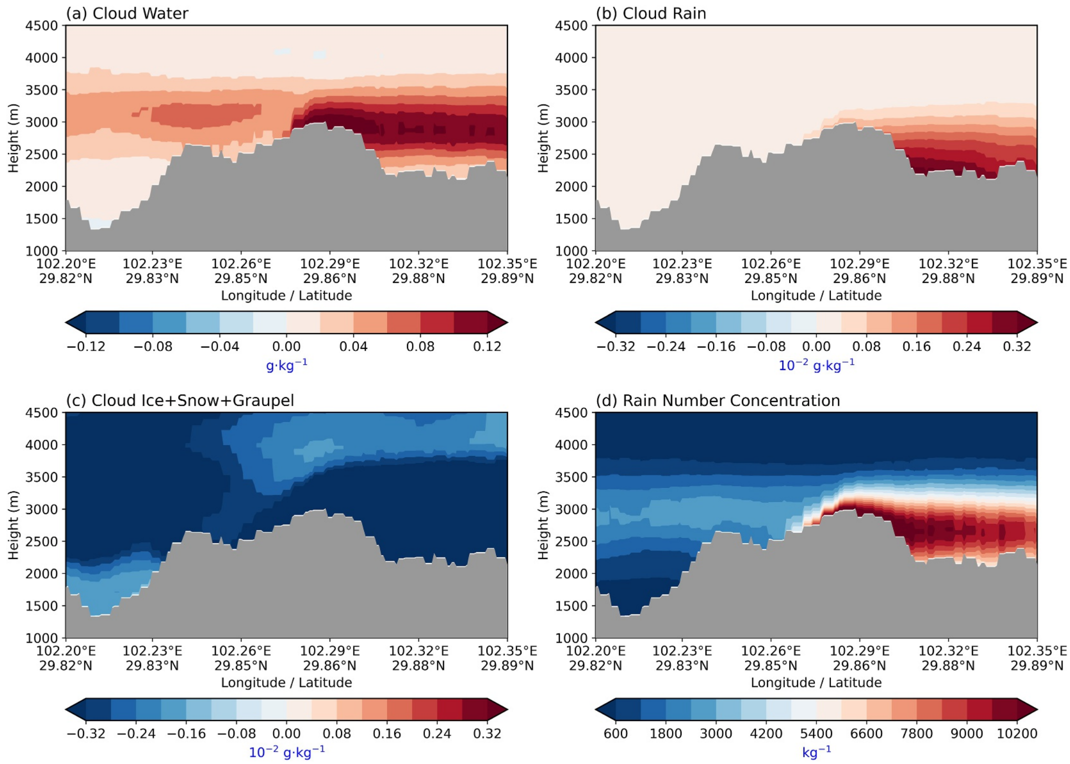

Figure 9. Time-mean cross sectional differences (Morrison-Thompson) in (a) cloud water, (b) cloud rain, (c) solid hydrometeors (cloud ice + snow + graupel), and (d) rain number concentration, derived from WRF simulations using the Morrison and Thompson schemes, averaged over eight icing events, along the airflow pathway shown in Figure 7 in domain d04. Gray shading denotes the underlying terrain.

droplet number concentration and shifting it toward smaller sizes, thereby suppressing the conversion of cloud water to cloud rain and solid hydrometeors relative to adopting the Thompson scheme. As a result, more cloud water is retained in the liquid water phase for a longer duration. This enhanced reservoir of super-cooled liquid water further promotes droplet collision and freezing on the conductor surface, leading to a significant increase in simulated icing thickness under the Morrison scheme is used.

5. Conclusion and Discussion

The mountainous regions of southwest Sichuan, China frequently experience power line icing, posing significant risks to the safe and stable operation of the power system. Numerical simulation provides an effective approach for predicting regional power line icing processes, thereby reducing economic losses and enhancing operational safety. However, the applicability of the Makkonen model driven by the WRF output in simulating power line icing in this region remains uncertain. To address this issue, this study conducted a series of numerical experiments using the WRF and Makkonen models with four nested domains using the Thompson and Morrison cloud microphysical schemes separately, based on eight observed icing events at the Erlangshan station. The main findings are given as follows:

The Makkonen model driven by the WRF output can reasonably reproduce the power line icing process in the mountainous regions of southwestern Sichuan. However, the simulated icing thickness generally exhibits an overall underestimation. Increasing the horizontal resolution of the WRF model improves the representation of near-surface air temperature and moisture and enhances the accuracy of icing thickness simulations. In addition, the Makkonen model driven by the WRF output using the Morrison scheme produces larger icing thickness than adopting the Thompson scheme, with results that are closer to observations.

The improvement associated with higher horizontal resolution is primarily linked to a more realistic representation of complex terrain. Finer resolution better captures terrain-induced cooling, wind acceleration, and

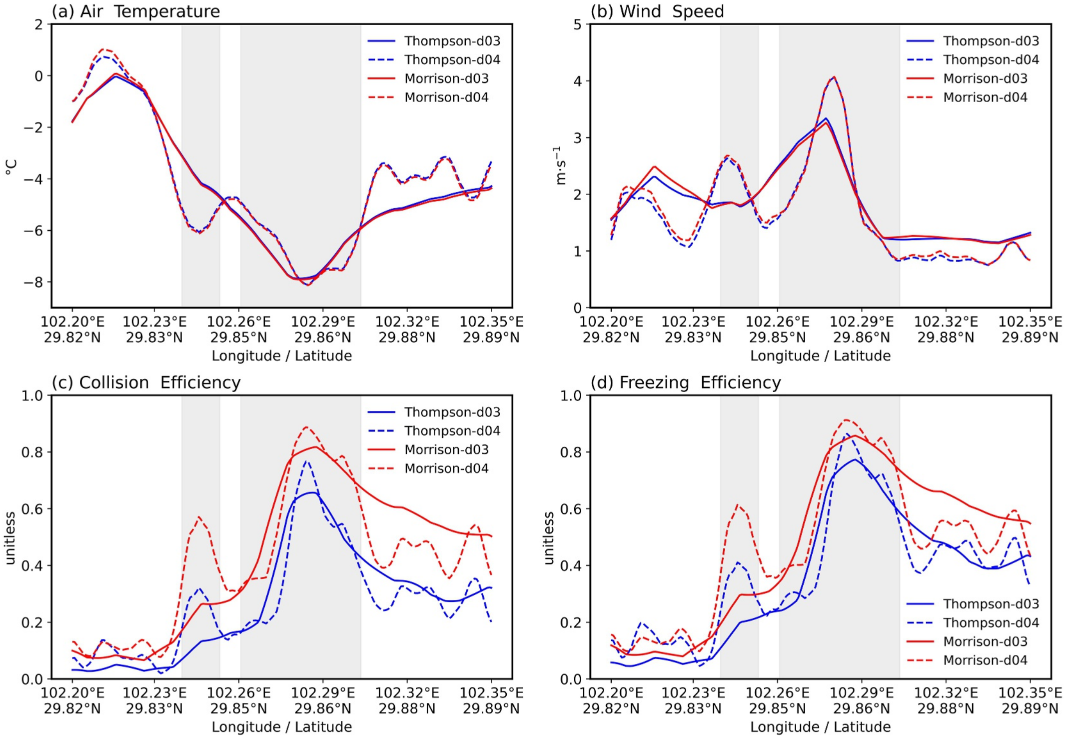

Figure 10. Time-mean cross sections of near-surface air temperature (a), wind speed (b), collision efficiency (c), and freezing efficiency (d) along the airflow pathway shown in Figure 7, averaged over the eight icing events. The fields are derived from the WRF simulations using the Thompson and Morrison schemes in domains d03 and d04. Gray shading denotes regions with terrain elevations greater than or equal to 2,500 m.

orographic lifting along mountain ridges. These dynamical effects promote the formation of super-cooled liquid water and enhance both collision and freezing efficiencies, leading to increased icing growth. As a result, the simulated icing thickness increases and the model bias is reduced.

Moreover, the differences between adopting the Morrison and Thompson schemes are mainly driven by microphysical processes. Adopting the Morrison scheme increases the rain number concentration and shifts the particle size distribution toward smaller droplets, thereby reducing the efficiency of conversion from cloud water to rainwater and solid hydrometeors. This leads to a greater retention of super-cooled liquid water and enhances collision and freezing efficiencies. Consequently, the Makkonen model driven by the WRF output using the Morrison scheme produces thicker icing and a smaller discrepancy between simulations and observations relative to adopting the Thompson scheme.

It should be noted that the evaluation in this study relies on observations from a single station, which may limit the spatial representativeness of the results. Although the Erlangshan station is located in a region with complex terrain and frequent icing events, local meteorological conditions can be strongly influenced by terrain-induced variability. As a result, the agreement between simulations and observations at this site may not fully reflect model performance across the broader mountainous region of southwestern Sichuan. This limitation implies that the conclusions regarding the impacts of horizontal resolution and microphysical schemes should be interpreted with caution when applied to other locations with different terrain characteristics or climatic conditions.

Future studies should place greater emphasis on improving the representation of near-surface liquid water content, which has been identified as a key factor controlling power line icing simulation (Chai et al., 2023; Drage & Hauge, 2008; Hou et al., 2024; Sokolov et al., 2025). At present, substantial uncertainties remain in both model configuration and cloud microphysical parameterization, particularly in complex terrain, largely due to the limited availability of direct liquid water observation (Nygaard et al., 2011, 2013, 2017; Sokolov et al., 2025; Yuan et al., 2025). The planned deployment of an advanced liquid water observation system at the Erlangshan station will provide a valuable opportunity to address this gap. These enhanced observations are expected to support more detailed investigation of the microphysical processes governing icing formation, facilitate the refinement of model parameterization, and ultimately improve the reliability of numerical icing simulation. Such advancements will contribute to more robust scientific guidance for the planning, design, and operation of power transmission lines in mountainous regions.

Conflict of Interest

The authors declare no conflicts of interest relevant to this study.

Availability Statement

The data used in this study includes: the SRTM terrain elevation data (Jarvis et al., 2008), the ERA5 reanalysis data (Hersbach et al., 2020), and the MODIS land cover data (Friedl et al., 2010). The filed observation data at the Erlangshan station can be obtained upon reasonable request. The code of the WRF v4.2 is publicly available at https://github.com/wrf-model/WRF/releases.

Acknowledgments
This work is funded by the Sichuan Science and Technology Program under Grant 2024YFFK0411, National Natural Science Foundation of China under Grant 42375157, and the Jiangsu Collaborative Innovation Center for Climate Change. We appreciate the High Performance Computing Center of Nanjing University.

References

Bartier, P. M., & Keller, C. P. (1996). Multivariate interpolation to incorporate thematic surface data using inverse distance weighting (IDW). *Computers and Geosciences*, *22*(7), 795–799. https://doi.org/10.1016/0098-3004(96)00021-0

Cai, S., Huang, A., Zhu, K., Guo, W., Wu, Y., & Gu, C. (2023). The forecast skill of the summer precipitation over Tibetan Plateau improved by the adoption of a 3D sub-grid terrain solar radiative effect scheme in a convection-permitting model. *Journal of Geophysical Research: Atmospheres*, *128*(11), e2022JD038105. https://doi.org/10.1029/2022JD038105

Cai, S., Zhu, K., Huang, A., Gu, C., Wu, Y., Zhu, X., & Zhao, W. (2025). Impacts of local and remote sub-grid terrain solar radiative effect on the Meiyu rainfall forecast in the Yangtze-Huaihe River Basin, China. *Journal of Geophysical Research: Atmospheres*, *130*(22), e2025JD044324. https://doi.org/10.1029/2025JD044324

Chai, H., Zhang, H., Wang, Q., Su, H., Yang, Y., & Gao, Z. (2023). Spatial and temporal distribution characteristics, Numerical Simulation and weather science causes of a large Scale icing process on UHV transmission lines in Yunnan-Guizhou Plateau. *Plateau Meteorology*, *42*(2), 359–373. https://doi.org/10.7522/j.issn.1000-0534.2021.00107

Chang, S. E., Mcdaniels, T. L., Mikawoz, J., & Peterson, K. (2007). Infrastructure failure interdependencies in extreme events: Power outage consequences in the 1998 ice storm. *Natural Hazards*, *41*(2), 337–358. https://doi.org/10.1007/s11069-006-9039-4

Chen, F., & Dudhia, J. (2001). Coupling an advanced land surface-hydrology model with the Penn State-NCAR MM5 modeling system. Part I: Model implementation and sensitivity. *Monthly Weather Review*, *129*(4), 569–585. https://doi.org/10.1175/1520-0493(2001)129<0569:CAALSH>2.0.CO;2

Cheng, X., Shi, F., Liu, Y., Liu, X., & Huang, L. (2022). Wind turbine blade icing detection: A federated learning approach. *Energy*, *254*, 124441. https://doi.org/10.1016/j.energy.2022.124441

Collins, W. D., Rasch, P. J., Boville, B. A., Hack, J. J., McCaa, J. R., Williamson, D. L., et al. (2004). Description of the NCAR community atmosphere model (CAM 3.0). *NCAR Tech. Note NCAR/TN-464+ STR*, *226*, 1326–1334. https://doi.org/10.5065/D63N21CH

Drage, M. A., & Hauge, G. (2008). Atmospheric icing in a coastal mountainous terrain. Measurements and numerical simulations, a case study. *Cold Regions Science and Technology*, *53*(2), 150–161. https://doi.org/10.1016/j.coldregions.2007.12.003

Duan, X., Duan, W., Xing, D., & Zhang, Y. (2018). The relationship between Kunming quasi-stationary front and Yunnan-Guizhou Plateau terrain. *Plateau Meteorology*, *37*(1), 137–147.

Friedl, M. A., Sulla-Menashe, D., Tan, B., Schneider, A., Ramankutty, N., Sibley, A., & Huang, X. (2010). MODIS Collection 5 global land cover: Algorithm refinements and characterization of new datasets. *Remote Sensing of Environment*, *114*(1), 168–182. https://doi.org/10.1016/j.rse.2009.08.016

Gettelman, A., & Morrison, H. (2015). Advanced two-moment bulk microphysics for global models. Part I: Off-line tests and comparison with other schemes. *Journal of Climate*, *28*(3), 1268–1287. https://doi.org/10.1175/jcli-d-14-00102.1

Grell, G. A., & Freitas, S. R. (2014). A scale and aerosol aware stochastic convective parameterization for weather and air quality modeling. *Atmospheric Chemistry and Physics*, *14*(10), 5233–5250. https://doi.org/10.5194/acp-14-5233-2014

Guo, L., Guo, Y., & Wang, J. (2019). Geological hazard analysis of poles and towers in Tibet section of Sichuan-Tibet transmission line. *Yunnan Water Power*, *35*(1), 17–19.

Hersbach, H., Bell, B., Berrisford, P., Hirahara, S., Horanyi, A., Munoz-Sabater, J., et al. (2020). The ERA5 global reanalysis [Dataset]. *Quarterly Journal of the Royal Meteorological Society*, *146*(730), 1999–2049. https://doi.org/10.1002/qj.3803

Hou, H., Wang, Y., Bai, X., Lv, J., Cui, R., Zhang, L., et al. (2024). Modelling icing growth on overhead transmission lines: Current advances and future directions. *Energy Conversion and Economics*, *5*(6), 343–357. https://doi.org/10.1049/enc2.12131

Hou, H., Yin, X., You, D., Chen, Q., Tong, G., Zheng, Y., & Shao, D. (2009). Analysis of the defects of power equipment in the 2008 snow disaster in Southern China Area. *High Voltage Engineering*, *35*, 584–590.

Hu, X., Wei, X., & Chen, B. (2006). Recent progress in anti-icing coating for transmission line. *Materials Protection*, *39*(3), 36–38.

Huang, A., Zhao, Y., Zhou, Y., Yang, B., Zhang, L., Dong, X., et al. (2016). Evaluation of multisatellite precipitation products by use of ground-based data over China. *Journal of Geophysical Research: Atmospheres*, *121*(18), 10–654. https://doi.org/10.1002/2016JD025456

Huang, A. N., Lazhu, Wang, J. B., Dai, Y. J., Yang, K., Wei, N., et al. (2019). Evaluating and improving the performance of three 1D Lake models in a large deep lake of the central Tibetan Plateau. *Journal of Geophysical Research: Atmospheres*, *124*(6), 3143–3167. https://doi.org/10.1029/2018jd029610

Huang, Q., Wang, J., & Ou, M. (2005). Analysis on accidents caused by icing damage in hunan power grid in 2005 and its countermeasures. *Power System Technology*, *29*(24), 16–19.

Huang, X., & Li, J. (2012). Icing thickness prediction model using BP Neural Network. In *2012 IEEE international conference on condition monitoring and diagnosis* (pp. 758–760).

Janjić, Z. I. (1994). The step-mountain eta coordinate model: Further developments of the convection, viscous sublayer, and turbulence closure schemes. *Monthly Weather Review*, *122*(5), 927–945. https://doi.org/10.1175/1520-0493(1994)122<0927:TSMECM>2.0.CO;2

Jarvis, A., Reuter, H. I., Nelson, A., & Guevara, E. (2008). The Shuttle Radar Topography Mission (SRTM) 90 m Digital Elevation Database v4.1 [Dataset]. *International Centre for Tropical Agriculture (CIAT)*. Retrieved from https://developers.google.com/earth-engine/datasets/catalog/CGIAR_SRTM90_V4

Jiang, X., Xiang, Z., Zhang, Z., Hu, J., Hu, Q., & Shu, L. (2014). Predictive model for equivalent ice thickness load on overhead transmission lines based on measured insulator string deviations. *IEEE Transactions on Power Delivery*, *29*(4), 1659–1665. https://doi.org/10.1109/TPWRD.2014.2305980

Jones, T. A., Skinner, P., Knopfmeier, K., Mansell, E., Minnis, P., Palikonda, R., & Smith Jr., W. (2018). Comparison of cloud microphysics schemes in a warn-on-forecast System using synthetic satellite objects. *Weather and Forecasting*, *33*(6), 1681–1708. https://doi.org/10.1175/waf-d-18-0112.1

Khain, A. P., Beheng, K. D., Heymsfield, A., Korolev, A., Krichak, S. O., Levin, Z., et al. (2015). Representation of microphysical processes in cloud-resolving models: Spectral (bin) microphysics versus bulk parameterization. *Reviews of Geophysics*, *53*(2), 247–322. https://doi.org/10.1002/2014rg000468

Li, Z., Bai, X., Zhou, Z., Hu, Z., Xu, J., & Li, X. (2008). Prevention and treatment methods of ice coating in power networks and its recent Study. *Power System Technology*, *32*(4), 7–13.

Lim, K. S. S., & Hong, S. Y. (2010). Development of an effective double-moment cloud microphysics scheme with prognostic cloud condensation nuclei (CCN) for weather and climate models. *Monthly Weather Review*, *138*(5), 1587–1612. https://doi.org/10.1175/2009mwr2968.1

Liu, D., & Niu, S. (2015). Observational study on real-time meteorological conditions during two wire icing processes. *Transactions of Atmospheric Sciences*, *38*(3), 428–432.

Long, L., Hu, Y., Li, J., & Hu, T. (2006). Study on statistic analysis of icing faults on transmission line and its preventive measures. *Electrical Equipment*, *7*(12), 26–28.

Luo, J., Huang, A., Jiang, X., Xu, M., Miao, X., Gu, C., & Zhu, X. (2025). The cold biases in the soil and surface air temperature simulations of RegCM4.7 model over the Tibetan Plateau in cold seasons reduced by adopting an improved snow cover fraction scheme. *Journal of Geophysical Research: Atmospheres*, *130*(8), e2025JD043507. https://doi.org/10.1029/2025JD043507

Luo, J., Huang, A., Lyu, S., Lin, Z., Gu, C., Li, Z., et al. (2023). Improved performance of CLM5. 0 model in frozen soil simulation over Tibetan plateau by implementing the vegetation emissivity and gravel hydrothermal schemes. *Journal of Geophysical Research: Atmospheres*, *128*(6), e2022JD038021. https://doi.org/10.1029/2022JD038021

Ma, X., Yang, K., La, Z., Lu, H., Jiang, Y., Zhou, X., et al. (2022). Importance of parameterizing lake surface and internal thermal processes in WRF for simulating freeze onset of an alpine deep lake. *Journal of Geophysical Research: Atmospheres*, *127*(18), e2022JD036759. https://doi.org/10.1029/2022JD036759

Makkonen, L. (1989). Estimation of wet snow accretion on structures. *Cold Regions Science and Technology*, *17*(1), 83–88. https://doi.org/10.1016/s0165-232x(89)80018-7

Makkonen, L. (1998). Modeling power line icing in freezing precipitation. *Atmospheric Research*, *46*(1–2), 131–142. https://doi.org/10.1016/s0169-8095(97)00056-2

Makkonen, L., & Wichura, B. (2010). Simulating wet snow loads on power line cables by a simple model. *Cold Regions Science and Technology*, *61*(2–3), 73–81. https://doi.org/10.1016/j.coldregions.2010.01.008

Makkonen, L., Zhang, J., Karlsson, T., & Tiihonen, M. (2018). Modelling the growth of large rime ice accretions. *Cold Regions Science and Technology*, *151*, 133–137. https://doi.org/10.1016/j.coldregions.2018.03.014

Morrison, H., Thompson, G., & Tatarskii, V. (2009). Impact of cloud microphysics on the development of trailing stratiform precipitation in a simulated squall line: Comparison of one- and two-moment schemes. *Monthly Weather Review*, *137*(3), 991–1007. https://doi.org/10.1175/2008MWR2556.1

Musilek, P., Arnold, D., & Lozowski, E. P. (2009). An ice accretion forecasting system (IAFS) for power transmission lines using numerical weather prediction. *Scientific Online Letters on the Atmosphere Sola*, *5*(1), 25–28. https://doi.org/10.2151/sola.2009-007

Niu, S., Zhou, Y., Jia, R., Yang, J., Lyu, J., Ke, Y., et al. (2011). Preliminary study of the microphysics of ice accretion on wires: Observations and simulations. *Science China Earth Sciences*, *41*(12), 1812–1821.

Nygaard, B. E. K., Ágústsson, H., & Somfalvi-Tóth, K. (2013). Modeling wet snow accretion on power lines: Improvements to previous methods using 50 years of observations. *Journal of Applied Meteorology and Climatology*, *52*(10), 2189–2203. https://doi.org/10.1175/jamc-d-12-0332.1

Nygaard, B. E. K., Byrkjedal, Ø., Iversen, E., Fredbo, M., Ágústsson, H., Welgaard, Ø., & Mc Innes, H. (2017). Development of a reliable modelling system for the calculation of rime ice loads on overhead transmission lines. *Proceedings–IWAIS*.

Nygaard, B. E. K., Kristjánsson, J. E., & Makkonen, L. (2011). Prediction of In-Cloud icing conditions at ground level using the WRF model. *Journal of Applied Meteorology and Climatology*, *50*(12), 2445–2459. https://doi.org/10.1175/JAMC-D-11-054.1

Podolskiy, E. A., Nygaard, B. E. K., Nishimura, K., Makkonen, L., & Lozowski, E. P. (2012). Study of unusual atmospheric icing at Mount Zao, Japan, using the Weather Research and Forecasting model. *Journal of Geophysical Research*, *117*(D12), D12106. https://doi.org/10.1029/2011jd017042

Poots, G. (2000). Ice and snow accretion on structures. *Philosophical Transactions of the Royal Society of London. Series A, Mathematical and Physical Sciences*, *358*, 2799–3033.

Seiki, T., Roh, W., & Satoh, M. (2022). Cloud microphysics in global cloud resolving models. *Atmosphere-Ocean*, *60*(3–4), 477–505. https://doi.org/10.1080/07055900.2022.2075310

Sokolov, P., Virk, M. S., Han, X., Nygaard, B. E., Molkoselkä, E. O., Kaikkonen, V. A., & Mäkynen, A. J. (2025). Field measurements of icing parameters and their application towards ice load maps: An overview. *Cold Regions Science and Technology*, *239*, 104579. https://doi.org/10.1016/j.coldregions.2025.104579

Tan, G., Yan, J., & Zhu, R. (1985). *Applied climatology* (pp. 3–56). Shanghai Science and Technology Press.

Thompson, G., Field, P. R., Rasmussen, R. M., & Hall, W. D. (2008). Explicit forecasts of winter precipitation using an improved bulk microphysics scheme. Part II: Implementation of a new snow parameterization. *Monthly Weather Review*, *136*(12), 5095–5115. https://doi.org/10.1175/2008MWR2387.1

Thompson, G., Politovich, M. K., & Rasmussen, R. M. (2017). A numerical weather model's ability to predict characteristics of aircraft icing environments. *Weather and Forecasting*, *32*(1), 207–221. https://doi.org/10.1175/waf-d-16-0125.1

Wang, H., Zhang, Y., Lin, W., & Wei, W. (2023). Transregional electricity transmission and carbon emissions: Evidence from ultra-high voltage transmission projects in China. *Energy Economics*, *123*, 106751. https://doi.org/10.1016/j.eneco.2023.106751

Wang, S. (1993). *Study of the wire ice coating in the high altitude regions of Yunnan province* (pp. 7–44). Yunnan Science and Technology Press.

Wang, Y., Xu, C., & Yuan, P. (2022). Is there a grid-connected effect of grid infrastructure on renewable energy generation? Evidence from China's upgrading transmission lines. *Energy and Environment*, *33*(5), 975–995. https://doi.org/10.1177/0958305x211031015

Wang, Z. (2011). Climate characters and changes of ice-freezing days in China. *Chinese Journal of Atmospheric Sciences*, *35*(3), 411–421.

Watanabe, Y. (1978). Flashover tests of insulators covered with ice or snow. *IEEE Transactions on Power Apparatus and Systems*, *97*(5), 1788–1793. https://doi.org/10.1109/tpas.1978.354672

Weng, B., Gao, W., Zheng, W., & Yang, G. (2021). Newly designed identifying method for ice thickness on high-voltage transmission lines via machine vision. *High Voltage*, *6*(5), 904–922. https://doi.org/10.1049/hve2.12086

Xie, Y., & Wang, J. (2013). Study on spatiotemporal distribution of conductor icing in southwestern Sichuan. *Electric power*, *46*(3), 30–34.

Xu, P., & Cheng, Y. (2017). A study on disaster-resistant design of power transmission lines based on actual statistical data. *Electronics World*, *23*, 156–157.

Xu, X., Huang, A., Zhang, Y., Yang, X., & Zhao, W. (2025). Impact of large-scale topography surrounding the Sichuan Basin on its regional hourly extreme precipitation in summer under specific weather patterns: Multi-case study. *Journal of Geophysical Research: Atmospheres*, *130*(9), e2024JD042239. https://doi.org/10.1029/2024JD042239

Xu, X., Huang, A., Zhao, W., Yang, B., Xue, D., & Zhang, Y. (2024). Roles of the Tibetan Plateau and Yunnan-Guizhou Plateau in the regional extreme precipitation over Sichuan Basin in summer: A case study. *Journal of Geophysical Research: Atmospheres*, *129*(3), e2023JD039776. https://doi.org/10.1029/2023JD039776

Yan, X., Wu, Z., & Gu, S. (2009). Analyses on the space-time distribution characteristics and their influence factors of freezing rain in Guizhou Province. *Plateau Meteorology*, *28*(3), 694–701.

Yang, J., Li, Z., Yang, F., & Huang, T. (2008). Analysis of the features of covered ice and collapsed Tower of transmission line snow and ice attacked in 2008. *Advances of Power System & Hydroelectric Engineering*, *24*(4), 4–8.

Yuan, M., Lv, A., Wang, W., Dong, X., & Ping, F. (2025). The microphysical properties and processes in in-flight icing: A case study. *Atmospheric Research*, *326*, 108326. https://doi.org/10.1016/j.atmosres.2025.108326

Zhang, Q., Chen, X., Ma, Y., Cao, D., Yang, B., Wen, J., et al. (2025). Integrating optimized cumulus and TOFD schemes for heavy precipitation forecasting in the Yarlung Tsangbo Grand Canyon. *Climate Dynamics*, *63*(1), 27. https://doi.org/10.1007/s00382-024-07503-9

Zhang, X., Huang, A., Yang, X., Gu, C., Cai, S., & Luo, J. (2024). Performance of Common Land Model in simulating the land surface thermal and hydrological processes over China improved by including the sub-grid terrain solar radiative effect. *Journal of Geophysical Research: Atmospheres*, *129*(24), e2023JD039775. https://doi.org/10.1029/2023JD039775

Zhang, Y., Xue, M., Zhu, K., & Zhou, B. (2019). What is the main cause of diurnal variation and nocturnal peak of summer precipitation in Sichuan Basin, China? The key role of boundary layer low-level jet inertial oscillations. *Journal of Geophysical Research: Atmospheres*, *124*(5), 2643–2664. https://doi.org/10.1029/2018JD029834

Zhao, Z., Huang, A., Ma, W., Wu, Y., Wen, L., Lazhu, & Gu, C. (2022). Effects of Lake Nam Co and surrounding terrain on extreme precipitation over Nam Co basin, Tibetan Plateau: A case study. *Journal of Geophysical Research: Atmospheres*, *127*(10), e2021JD036190. https://doi.org/10.1029/2021JD036190

Zhou, X., Liu, L., Wang, S., Shao, X., Li, T., Wang, Z., et al. (2021). An overview on characteristics, tendency, and prediction technology of natural disaster in Zhejiang power grid. *Zhejiang Electric Power*, *40*(5), 20–29.

Zhou, X., Yang, K., & Wang, Y. (2018). Implementation of a turbulent orographic form drag scheme in WRF and its application to the Tibetan Plateau. *Climate Dynamics*, *50*(7), 2443–2455. https://doi.org/10.1007/s00382-017-3677-y